Bulletin of the Seismological Society of America, 90, 1, pp. 134–150, February 2000

3D Viscoelastic Wave Propagation in the Upper Borrego Valley, California, Constrained by Borehole and Surface Data

by K. B. Olsen, R. Nigbor, and T. Konno

Abstract We have simulated 2-Hz-wave propagation in a three-dimensional model of the upper Borrego Valley, southern California, for a **M** 4.9 earthquake with epicenter 5 km north of the valley. A 4th-order staggered-grid finite-difference method was used to calculate viscoelastic ground motion in a basin model (9 km by 5 km by 0.4 km) consisting of heterogeneous sediments surrounded by bedrock. We simulated the earthquake as a double-couple point source and computed the ground motions in the valley separately for the parts of the source incident from below and from the North. The earthquake was recorded by a surface array as well as a deep downhole array (0–238 m depth) in the center of the valley, all equipped with digital three-component seismic instruments. The simulation reproduces the overall pattern of ground motions at basin and borehole sites and shows a good correlation of observed to synthetic waveforms. In particular, the 3D simulation reproduces the recorded peak motions, cumulative kinetic energies, and Fourier spectral amplitudes within a factor of 2 for most components at the individual sites. The correlation between data and simulation allows us to identify the secondary arrivals in the records as Love and Rayleigh waves generated at the edges of the valley and the troughs of the basin. The peak velocities for the waves incident into the valley from below are generally more than an order of magnitude larger than those for the waves incident from the North. The success of the prediction requires the inclusion of anelastic attenuation in the simulation with Q values for P and S waves in the alluvium of about 30.

We also used a profile of the 3D model and the soil parameters at the deep borehole to examine the ability of 2.5D and 1D model approximations to predict the data. The maximum peak velocities and total cumulative kinetic energies are reproduced at the recording sites within a factor of 2 for both 2.5D and 1D model approximations, but are underpredicted by up to an order of magnitude at some depths for individual components. In particular, the 2.5D and 1D simulations tend to underpredict the duration.

Introduction

The recent appearance of more powerful computers, better constrained basin models, and more efficient numerical wave propagation codes have facilitated computation of the 3D low-frequency seismic response of numerous sedimentary basins throughout the world (e.g., Frankel and Vidale, 1992; Frankel, 1993; Yomogida and Etgen, 1993; Olsen and Schuster, 1994, 1995; Olsen *et al.,* 1995a,b; Olsen and Archuleta, 1996; Wald and Graves, 1998). Due to large computational requirements, the 3D simulations have generally been limited to unrealistically large minimum velocities (0.5–1 km/sec), and the bandwidth has generally been limited to frequencies less than 1 Hz. However, these studies demonstrated significant 3D effects from the basin structures, including a strong sensitivity of the shaking duration to the location in the basin and the generation of surface waves at the edges of the basin.

While the 3D basin studies are able to test absolute ground motions for simulations of specific events by comparison to surface recordings, uncertainty still remains about the relative contribution to the ground motion from the path effects from the source to the sedimentary basin and from the basin itself. Direct modeling of basin effects requires accurate information of the incident wavefield and parameters of the soil. The conventional assumption that surface rock recordings represent a mostly undistorted incoming wavefield was recently questioned due to the site response

of near-surface, altered bedrock (Steidl *et al.,* 1996). Instead, borehole recordings at levels below the sediments may provide the only reliable estimate of the incident wavefield.

The Borrego Valley seismic observatory represents an excellent site for testing the accuracy of state-of-the-art 3D wave-propagation techniques, with direct constraints on the incoming wavefield. The observatory is located in the northernmost part of the valley, hereafter denoted upper Borrego Valley. This part of the valley is limited in size to about 9 km by 5 km and is equipped with surface and downhole high-resolution three-component, digital seismic instrumentation, and the seismic velocities and densities of the underlying basin sediments have been accurately mapped by a variety of geophysical methods. The deepest borehole instrument is located 238 m below the valley's surface in the bedrock underlying the basin sediments. The initial arrivals recorded at this depth may therefore be taken as an approximation of the seismic waves impinging into the valley sediments from nearby earthquakes.

While significant 3D ground-motion amplification effects are reported for sedimentary basins throughout the world, an important question in ground motion modeling is to what extent the geometry of a specific sedimentary basin affects the ground motion. If it can be shown that the ground motion amplification due to the 3D basin structure is insignificant, or if 2.5D or even 1D approximations of the earth model appear sufficient to accurately model wave propagation, tremendous computer resources can be saved in future estimations of ground motion. Horike (1988), Horike *et al.* (1990), and Frankel (1993) showed that there can be major differences in the seismic response of 2D and 3D basin models. These differences include larger amplitudes and a longer duration of shaking obtained from 3D basin models compared to those obtained from 2D models. Olsen and Schuster (1995) found that 2D and especially 1D synthetics generally underestimate the peak velocities, cumulative kinetic energies, and mean spectral magnitudes predicted by 3D modeling for the Salt Lake Basin. While the relatively simple 3D Salt Lake Basin model consisted of homogeneous sediments surrounded by bedrock, the upper Borrego Valley model is much better constrained and therefore suited to accurately estimate the 2.5D and 3D amplification effects. In addition, the upper Borrego Valley has both surface and borehole recordings available for comparison with simulations.

Another critical issue for the ground-motion modeling is the effect of anelastic attenuation on the ground motion. The duration of shaking in alluvial valleys has been found to be strongly dependent on the anelastic attenuation (e.g., Olsen *et al.,* 1995a). Here we compare the results of 3D elastic and viscoelastic simulations with data at both surface and downhole recordings in order to estimate the effects of anelastic attenuation for the upper Borrego Valley.

Our main objective in this article is to assess the accuracy of purely deterministic ground motion predictions carried out using some of the most accurate information available on a subsurface velocity and density structure, and incoming wavefield for a **M** 4.9 scenario earthquake.

Wave Propagation in the Upper Borrego Valley

Upper Borrego Valley Model

The Borrego Valley is located in the desert of southern California in an area of relatively high seismicity, consisting mostly of right-lateral strike-slip events from northwest-striking faults (Fig. 1). For this reason, and due to the relatively small size of the valley and thickness of the underlying sediments (less than 400 m), the upper Borrego Valley was deployed with both a surface and downhole array of high-resolution three-component digital seismic instrumentation (Fig. 2).

The 3D model of the upper Borrego Valley consists of sediments surrounded by bedrock. The seismic velocities of the sediments and bedrock, as well as the configuration of the sediment/bedrock boundary were estimated by 3D inversion of gravity data and interpretation of seismic reflection and refraction lines and borehole logs from the downhole array (Agbabian Associates, 1996). Based on the surveys, the sediments are separated into unsaturated and saturated alluvium. *P*- and *S*-wave velocities and densities for the unsaturated alluvium vary between 0.5–1.2 km/sec, 0.3–0.65 km/sec, and 1.9–2.1 g/cm^3, respectively. *P*- and *S*-wave velocities and densities for the saturated alluvium vary between 1.9–2.3 km/sec, 0.65–0.8 km/sec, and 2.2–2.3 g/cm^3, respectively. The borehole was deployed with instruments at depths of 0 m, 9.4 m, 19.4 m, 138 m, and 238 m below the valley surface. The deepest instrument is located in bedrock, about 10 m below the lower boundary of the sediments (Fig. 2b). *P*- and *S*-wave velocities and densities for bedrock are 5.2 km/sec, 3.0 km/sec, and 2.65 g/cm^3, respectively. The elastic parameters below the main station are plotted in Figure 3.

Many previous 3D modeling studies have not included anelastic attenuation (e.g., Olsen and Schuster, 1994, 1995; Olsen *et al.,* 1995b, 1996). However, Frankel and Vidale (1992), Frankel (1993), and Olsen *et al.* (1995a) showed that attenuation is a major limiting factor to the duration and peak motion in alluvial valleys. Here, we simulate wave propagation for frequencies up to 2 Hz and a minimum shear-wave velocity of 0.3 km/sec, so we expect significant effects from attenuation in the upper Borrego Valley. Unfortunately, Q is the elastic parameter with the largest uncertainty in the upper Borrego Valley model. We used trial-and-error modeling to estimate the distributions of Q_s and Q_p that generate synthetics with an optimal fit to data, in particular for the amplitude of the reverberations following the initial arrival where anelastic attenuation is most effective. We find that values of both Q_s and Q_p of 30 in the sediments provide the best fit between synthetics and data (see Figure 3). Outside the sediments we used $Q_s = 0.1V_s$ (m/sec) and $Q_p = 1.5Q_s$. To our knowledge, this relation between Q and ve-

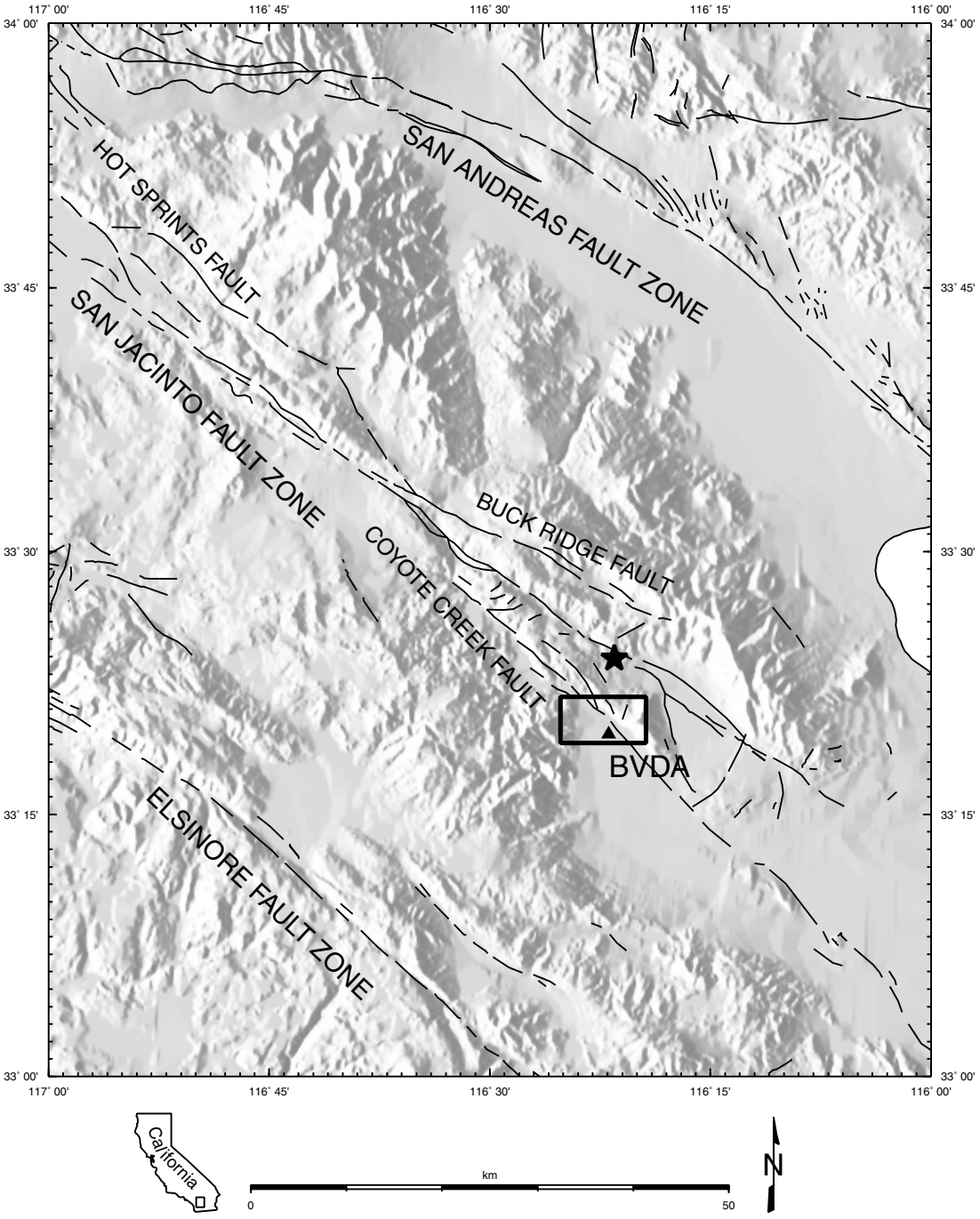

Figure 1. Location of the upper Borrego Valley. The triangle depicts the location of the downhole array. The star depicts the epicenter of the **M** 4.9 earthquake used in this study.

locity is commonly used in absence of better constraints. However, the effect of attenuation in the rock has limited effect on the ground motion.

Finite-Difference Scheme and Scenario Earthquake

We use a fourth-order staggered-grid finite-difference scheme (Olsen, 1994) to solve the 3D viscoelastic equations of motion (Blanch *et al.,* 1995; Robertsson *et al.,* 1994). Viscoelasticity is implemented using stress relaxation independently for P and S waves using a standard linear solid model with one relaxation peak. The accuracy for $Q_s = 100$ is estimated to be less than 5% for the central 1/3 of the bandwidth of interest, but decreases significantly toward the smallest and largest frequencies (see Blanch *et al.,* 1995,

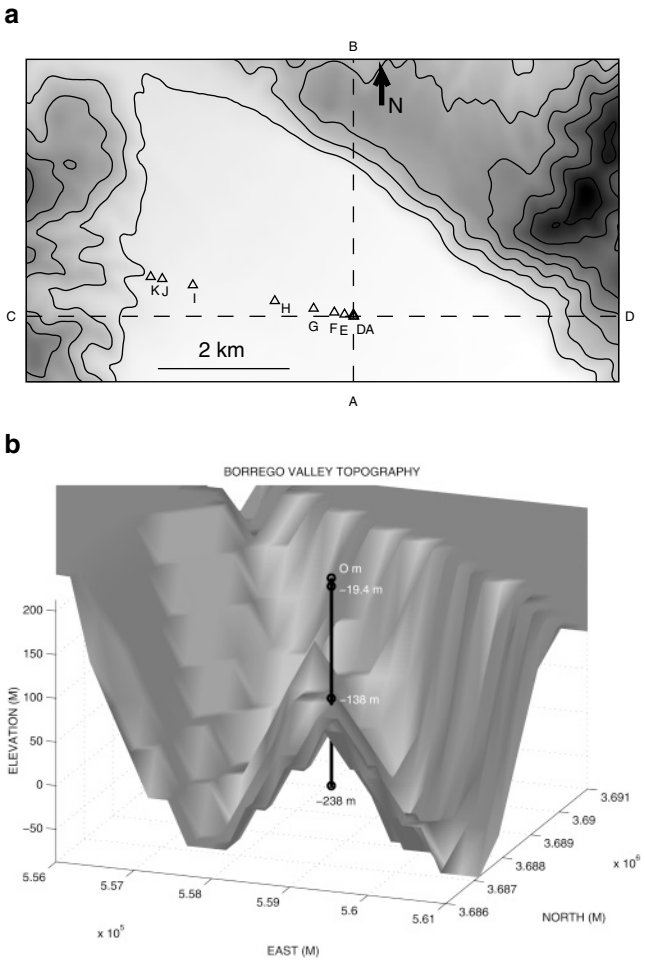

Figure 2. Borrego Valley model and seismic instrumentation. (a) Map of the Borrego Valley, as shown by the inset in Figure 1. The contours depict the surface topography with a contour spacing of 100 m. The triangles denote the locations of surface recording sites. The profiles A-B and C-D depict the location of the cross sections used for the 2.5D modeling and the line used to display source-time functions, respectively. (b) 3D perspective of the isosurface for V_s = 1 km/sec, superimposed with the borehole array. Note that the borehole array is located on a ridge in between two deeper troughs of the basin.

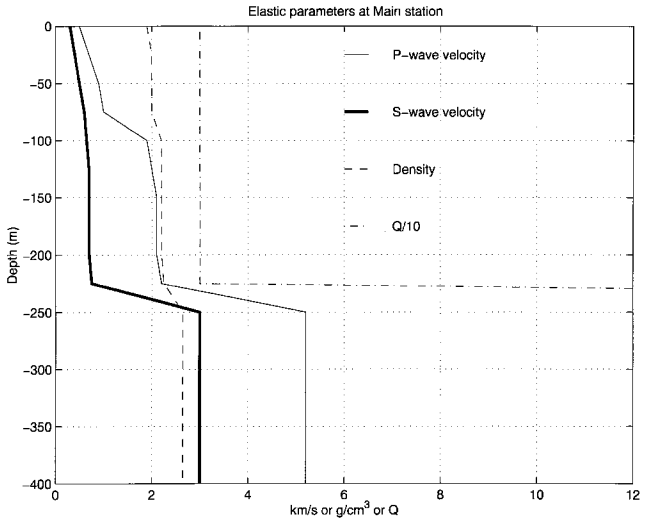

Figure 3. *P*- and *S*-wave velocities, densities, and *Q* profile at the main station.

Figure 4). This implementation differs from that presented by Graves (1996) where anelastic attenuation is applied at a single frequency without distinction between Q_s and Q_p. We use the absorbing boundary conditions by Clayton and Engquist (1977) and the sides of the computational model are padded with homogeneous regions of attenuative material to furthermore limit reflections from the boundaries of the grid (Cerjan *et al.,* 1985).

Our scenario earthquake is selected as the **M** 4.9 earthquake that occurred on 26 July 1997 with epicenter about 5 km north of the valley and a hypocentral depth of 12.9 km (see Figure 1). The earthquake was recorded by 11 surface stations and a deep and 2 shallow borehole arrays in the valley. We used at right-lateral strike-slip focal mechanism on a vertical fault with a strike of 306°. The focal depth and source mechanism is taken as a combination of estimates from the U.S. Geological Survey and the Southern California Earthquake Center. The strike is in agreement with the general trend of the Coyote Creek and San Jacinto faults (see Figure 1). The source parameters are listed in Table 1.

Simulation of Wave Propagation

We simulated the **M** 4.9 earthquake in a two-step procedure in a fashion similar to that obtained by a variable-grid finite-difference implementation. However, in order to demonstrate the relative contribution of energy impinging onto the upper Borrego Valley from below and from the north for the earthquake, we carried out two different sets of simulations (see Figure 4).

- First, a cosine-shaped double-couple point source-time function with a duration of 0.35 sec was inserted at the hypocenter location (see Figure 1, Table 2). We find that this source-time function generates a satisfactory fit between the initial arrival on the synthetics and data at the bottom of the deep borehole. The point source was simulated in two different models with a grid spacing of 100 m and *P*- and *S*-wave velocities and densities defined by the regional model by Hadley and Kanamori (1977), (1) one with absorbing boundary conditions and (2) one with a free surface at the top of the model. The stress tensor for the wavefield was saved at a sheet of node points located at a datum plane 400 m below the surface for simulation (1), just below the deepest sediments of the upper Borrego Valley model, and along a vertical sheet extending from the surface to a depth of 400 m for simulation (2). Figure 5 shows the particle velocities computed along the east-west profile C-D (see Figure 2a), 400 m below the valley floor. Note that the main station (at 5 km on Figure 5) is

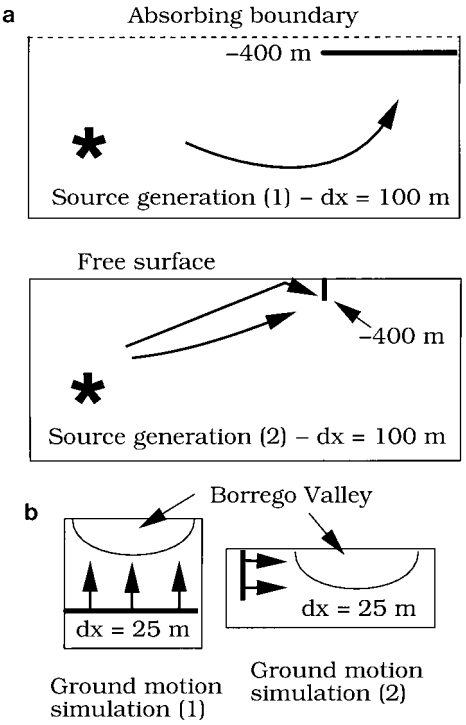

Figure 4. Illustration of the two-stage simulation technique used in this study. (a) First, a double-couple point source was inserted in models with a grid spacing of 100 m and (1) an absorbing and (2) a free-surface boundary condition at the upper edge of the grid. The stress tensor was saved along a horizontal plane at a vertical distance from the hypocenter corresponding to a depth of 400 m below the valley for (1), and along a vertical plane from the surface to a depth of 400 m below the valley for (2). (b) The stress-time histories from (a) were added to the stress tensor at the corresponding location in simulations with a grid spacing of 25 m, including the 3D Borrego Valley and a free-surface boundary condition at the upper grid boundary.

close to a nodal point with larger motion on the north-south component compared to that for the east–west component. This is in agreement with data, as seen in Figure 6 comparing the particle velocities below the main station to the deepest (-238 m) borehole recordings. There is a strong similarity between the computed particle velocity and the borehole recording for the direct arrival. The remaining energy in the deep borehole records represent reflections from the surface and reverberations in the overlying sediments.

- Secondly, the stress-time histories computed in the simulations (1) and (2) described above are added to the stress tensor at the appropriate datum planes in the 3D Borrego Valley velocity model with a grid spacing of 25 m. Using a modeling resolution of 5 points per wavelength (Levander, 1988), this discretization enables us to simulate wave propagation up to 2 Hz in a model where near-surface shear wavelengths are on the order of 150 m. The upper Borrego Valley model (approximately 9 km by 5 km by 1.25 km) is discretized into 361 by 201 by 51 ($=3.7$ million) grid points. The 3D modeling parameters are listed in Table 2.

Table 1
M 4.9 Source Parameters

Strike (degrees)	306
Dip (degrees)	90
Rake (degrees)	180
Moment (Nm)	$2.51 \cdot 10^{15}$
Depth (km)	12.9
Epicenter (lat, lon)	33.40, -116.35

Table 2
3D Viscoelastic Basin Modeling Parameters

	Simulations (1)*	Simulations (2)*
Spatial discretization (km)	0.1	0.025
Temporal discretization (sec)	0.0065	0.00225
Number of east-west grid points	240	401
Number of north-south grid points	160	237
Number of vertical grid points	200	50
East-west extent of model (km)	14	9
North-south extent of model (km)	16	4.9
Vertical extent of model (km)	20	1.2
Minimum source frequency (Hz)	0.0	0.0
Maximum source frequency (Hz)	2.0	2.0
Number of timesteps	1200	5000
Simulation time (sec)	7.8	11.25

*See Figure 4.

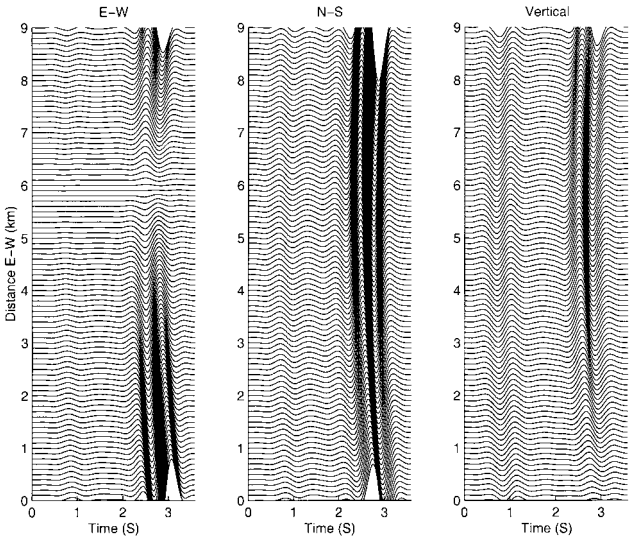

Figure 5. Source-time functions at a depth of 400 m below the Borrego Valley along profile C-D shown in Figure 2a.

Analysis of Simulated Wave Propagation

In this section, we use snapshots and peak particle velocity maps to analyze the simulated wave propagation for

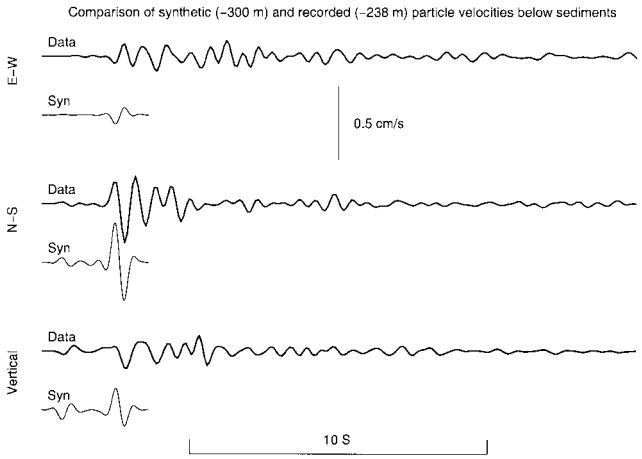

Figure 6. Comparison of simulated particle velocities at a depth of 300 m to recordings (thick traces) at the deepest borehole station (− 238 m).

the **M** 4.9 earthquake in the upper Borrego Valley. We use the simulation for the wavefield impinging onto the valley from below.

Figure 7 shows snapshots of particle velocities for approximately 10 sec of 2-Hz-wave propagation. The snapshots clearly show phases generated at the edges of the valley, in particular at the northwest–southeast trending edge, that propagate toward the southwest (see snapshots between 2.7 sec and 9.0 sec). These phases are a combination of Love and Rayleigh waves, as will be discussed in the following section. These surface waves interfere with scattered waves in the basin sediments, which becomes much more pronounced at later times. Note also how the waves are amplified above the two north–south trending troughs located in the southern part (Fig. 2b), especially apparent in the snapshots of the north–south component at 4.5–6.3 sec.

The peak velocities in the upper Borrego Valley are shown in Figure 8, superimposed with depth contours for the isosurface of V_s = 1 km/sec. The north–south component contains the strongest effects of the source (see Figure 5) and represents the largest peak velocities. Note the significant basin edge effects, in particular along the eastern boundary of the valley, as noticed in the snapshots (Fig. 7). Some of the largest amplitudes are found along the relatively steeply dipping eastern edge of the valley. This is in agreement with results from other 3D scenario modeling studies (e.g., Olsen *et al.,* 1995a; Olsen, 1999), where some of the strongest ground-motion amplifications were found near the steepest-dipping basin edges. Another striking pattern in the peak velocities is the increased amplification immediately behind convex-shaped parts of the basin edges or bottom (e.g., the north–south trending trough below station H). Such amplification pattern was noticed for 3D simulations of wave propagation in the Weber Basin, Utah (Olsen and Schuster, 1994) and identified as focusing effects at the convex-shaped boundaries of the basin. The reason why the focusing occurs for the wavefield impinging *from below* the valley is that the convex-shaped parts of the sediment-bedrock interface at the edge of the valley tend to maintain their cylindrical structure from the surface to a limited depth, dipping toward the center of the valley.

Comparison of Synthetics and Data

Surface and Borehole Instrumentation

The equipment at each station consists of Kinemetrics FBA-23 accelerometers (ALTUS series with 20-bit digital recording). We included data from the surface array for 11 stations, of which 10 (A–J) are located on unconsolidated sediments in the upper Borrego Valley and one (K) is located on a weathered bedrock outcrop in the mountains to the west of the valley (Figure 2 and Table 3). Borehole data is used at depths of 0 m, 9.4 m, 19.4 m, 138 m, and 238 m at the main station in the center of the valley, at a depth of 91 m at station J, and at a depth of 30 m at station K. The main station is located 10 m from the station A (omitted on Figure 2 for clarity).

Comparison of Simulated and Observed Earthquake Records

Now we examine the successes and failures of using the 3D viscoelastic simulation to predict 2-Hz ground motions in the upper Borrego Valley by comparing our synthetic seismograms to three-component records of the **M** 4.9 earthquake recorded by both the surface and downhole arrays (Table 3). The identification of phases is based on the relative amount of energy on the three components of motion and particle motions.

In order to illustrate the relative bandwidths of the data and simulations, Figure 9 shows the root mean square (rms) Fourier spectral amplitude for data and synthetics at the main station (surface). The data contains the largest spectral amplitudes below about 2 Hz, which is covered by the bandwidth of the simulations. However, the simulations omit a significant fraction of the energy in the data between 2 and 7 Hz.

Figure 10 compares observed 0.1–2 Hz velocity seismograms for the **M** 4.9 earthquake at surface stations to the synthetics for the waves impinging onto the valley from below and from the North. The observed traces are aligned with the simulated ones using the arrival with the largest amplitude, at about 3 sec on the north–south component. The observed seismograms show a good agreement in the maximum amplitudes, duration, and general waveforms of significant wave trains at most sites. Due to the relatively small distances between stations A and F (see Figure 2a), the waveforms recorded at these sites are similar. As expected, the best correlation of waveforms for the synthetics and data is obtained for the initial arrivals, which are predominantly controlled by the source, but later arriving phases are also well correlated. For example, the synthetics reproduce a sec-

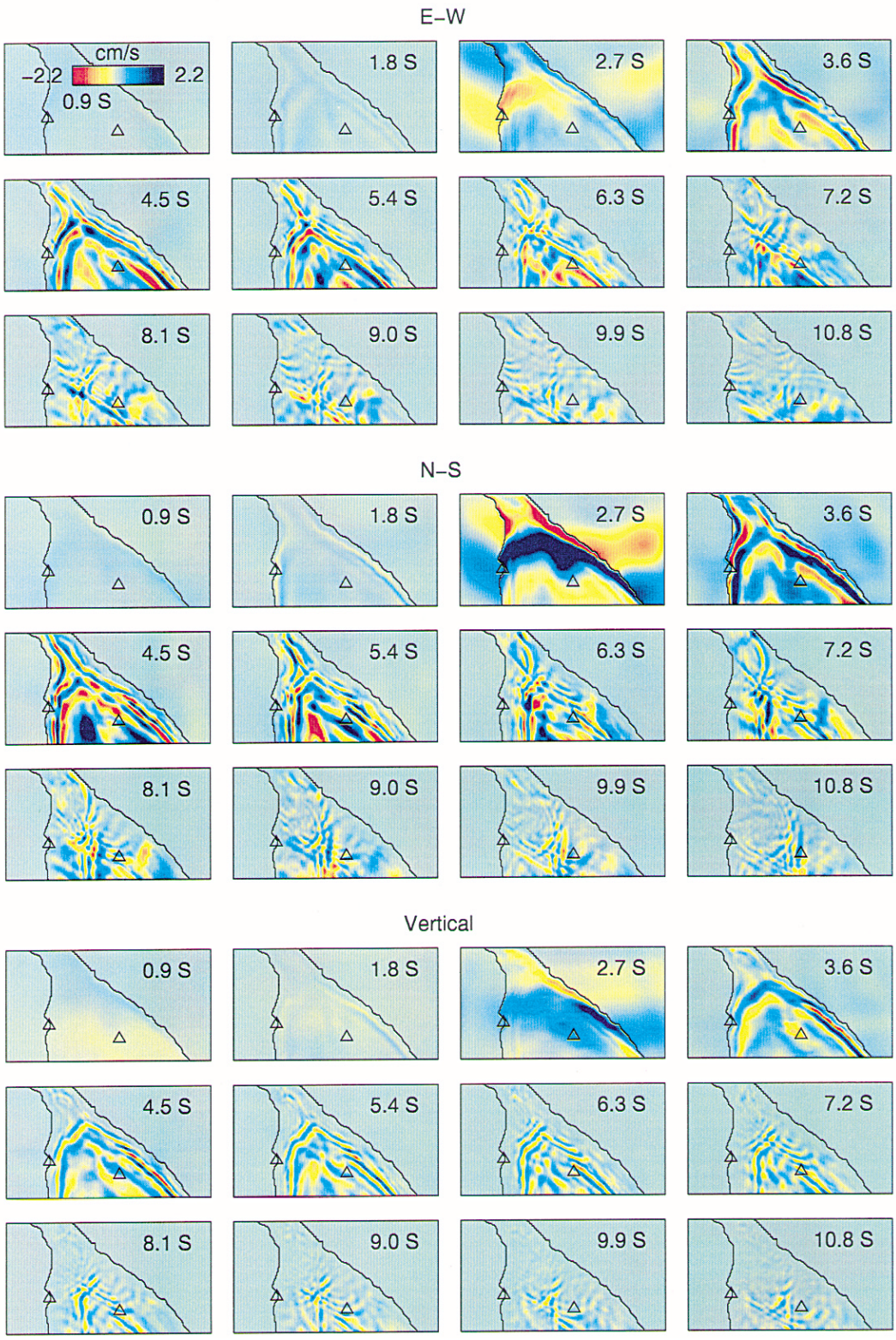

Figure 7. Snapshots of simulated wave propagation in the Borrego Valley for the **M** 4.9 earthquake. The snapshots depict particle velocities at 0.9-sec intervals for approximately 10 sec of wave propagation after the origin time of the earthquake. The triangles depict the location of the borehole array (main station) and the rock station. The thick line shown on the snapshots is the depth contour of 0.05 km for the isosurface of $V_s = 1$ km/sec and depicts the outline of valley. The particle motion is scaled by the same constant for all snapshots.

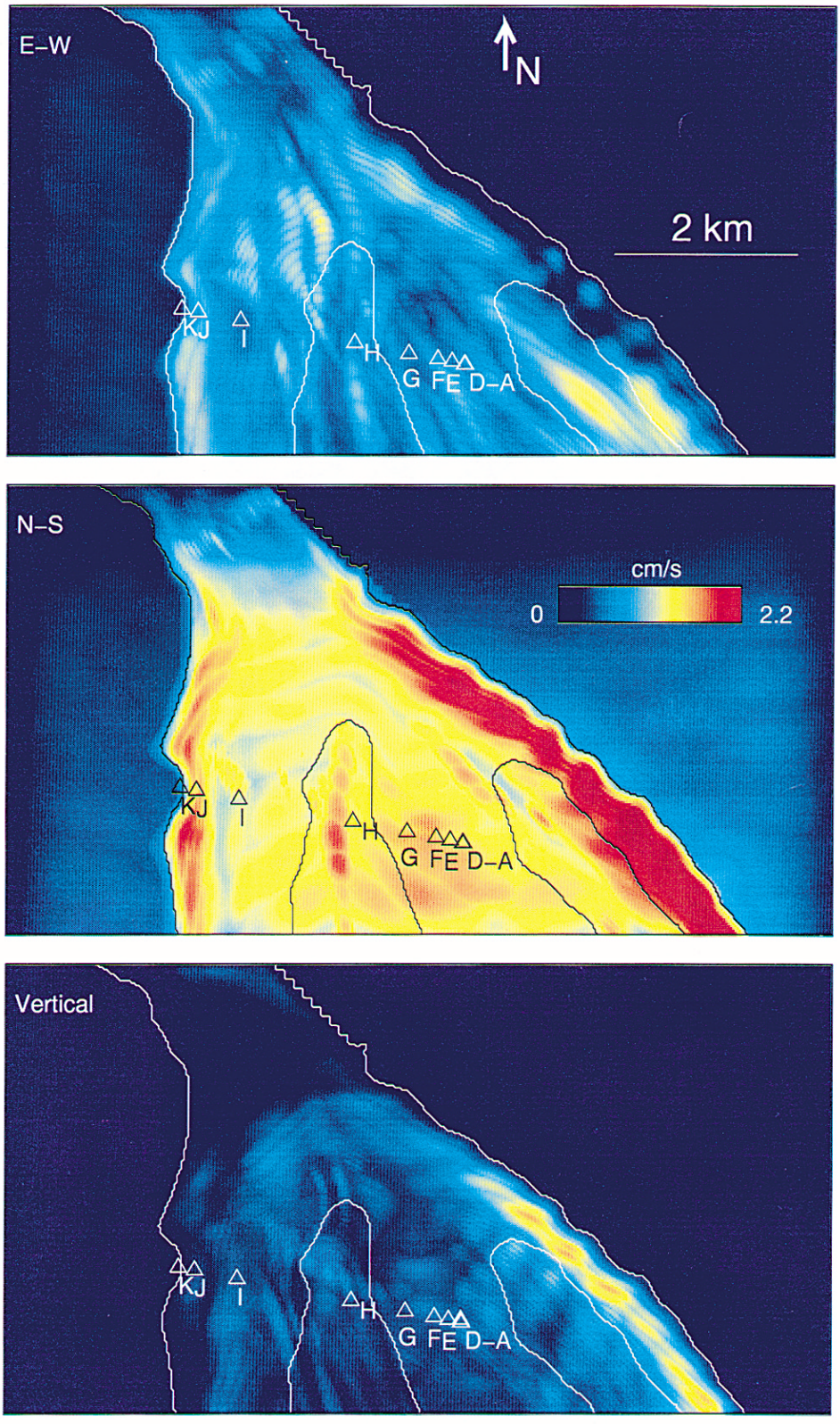

Figure 8. Maps of peak velocities in the Borrego Valley for a simulation of the **M** 4.9 earthquake, superimposed with the depth contours of 0.05 km and 0.3 km for the isosurface of V_s = 1 km/sec. The triangles depict the location of the borehole array and the rock station. The peak velocities are scaled by the same constant for all components.

Table 3
Stations Used to Record Seismic Waves from the **M** 4.9 Earthquake

Code	Lat (N)	Long (W)	Elev (m)	Material
Main	33 19 36.1879	116 21 58.3030	227	alluvium
Main	33 19 36.1879	116 21 58.3030	218	alluvium
Main	33 19 36.1879	116 21 58.3030	208	alluvium
Main	33 19 36.1879	116 21 58.3030	89	alluvium
Main	33 19 36.1879	116 21 58.3030	−11	bedrock
A	33 19 36.1899	116 21 58.6898	227	alluvium
B	33 19 36.1918	116 21 59.0766	228	alluvium
C	33 19 36.3581	116 21 59.8498	228	alluvium
D	33 19 36.6907	116 22 01.3937	228	alluvium
E	33 19 37.1926	116 22 04.2910	229	alluvium
F	33 19 38.1972	116 22 10.2790	231	alluvium
G	33 19 40.2071	116 22 22.4485	234	alluvium
H	33 19 44.0558	116 22 45.2419	239	alluvium
I	33 19 52.0869	116 23 33.3425	249	alluvium
J	33 19 55.2592	116 23 51.3073	260	alluvium
K	33 19 56.0048	116 23 58.0696	284	bedrock

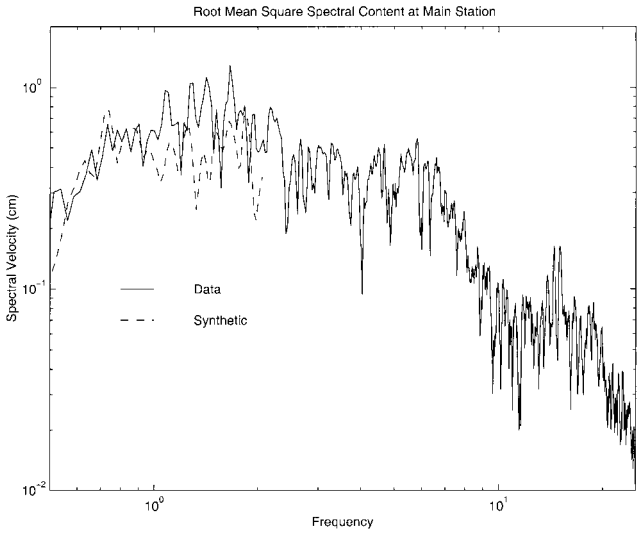

Figure 9. Root mean square spectral amplitudes for data and synthetics at the surface station of the deep borehole.

ondary arrival 2–3 sec after the initial *S* wave at stations A–F and H, particularly clear on the horizontal components. The snapshots in Figure 7 (3.6–4.5 sec) show that this phase is generated by conversion at the eastern slope of the easternmost trough of the basin, and the particle motion is that of predominantly Love/SH waves. This phase is followed by a Rayleigh wave generated at the eastern edge of the valley (arriving at about 7 sec at station A). The large-amplitude phase on the north–south component arriving at the main station (located 10 m from station A) at about 10 sec, also reproduced by the simulation, is identified as a Love wave generated at the western edge and nearby trough of the basin. At stations I and H, the relatively large-amplitude energy arriving at 3.5–5.5 sec is predominantly a Love wave with a smaller component of a Rayleigh wave, generated at the western edge of the basin. These phases are amplified within the deepest part of the western trough of the basin as well as by superposition of weaker surface waves arriving from northeastern and northwestern directions to generate the relatively large-amplitude phases at 7.6–9.0 and 9.7–11 sec at station H.

Although the general agreement between synthetics and data is good at some sites, the synthetics tend to somewhat underpredict the recorded durations, particularly on the east–west and vertical components. This discrepancy suggests a lack of complexity in the basin model.

The variation of peak velocities generally agree for synthetics and data across the surface array. The peak velocities for stations A–G in the center of the valley are characterized by relatively large values on the north–south component above the bedrock high shown in Figure 2b. At station H, the peak velocity increases in the simulation due to influence of the western trough of the basin (see Figure 8), in agreement with data. At station I, the peak velocity has decreased for both data and synthetics above the shallowing sediments toward the west (Figure 2b). The basin edge effect has increased the peak velocities on the synthetics at the shallow alluvium site J to values larger than those for the data, in particular for the east-west and vertical components, while peak velocities for data and synthetics at the rock site K are in much closer agreement. The discrepancy at station J is likely related to uncertainty of the shape of the nearby basin edge. Note also that the energy arriving from below is much stronger than that incident from North, as expected from the near-vertical incidence angle of the earthquake. For this reason, the synthetics for the wavefield impinging from below is very similar to the combined synthetics. The energy for the waves incident from the North tends to be larger for the deeper sediment sites toward the east (H and I). The Fourier spectra for data and synthetics at the surface stations for most frequencies show good correlation (Fig. 11).

A comparison of synthetics and data from the deep borehole is shown in Figure 12. The contribution to the synthetics from the wavefield arriving from the north is negligible below the surface and has been omitted. For clarity in the near-surface region, we omit data at 0 m and −19.4. However, the data at these stations are very similar to those shown at −9.4 m (see Figure 13). The synthetics reproduce the increase in amplitude for the data up through the sediments, reflecting the change in impedance and show good fits of waveform for data and synthetics, in particular for the first 5 sec. As observed for some of the surface stations, the synthetics somewhat underpredict the durations for some components.

Figure 14 compares synthetics to data at the shallow borehole stations J (0 m and −91 m) and K (0 m and −30 m). As noted in the comparison for the surface data, the synthetics tend to overpredict the amplitudes of the surface

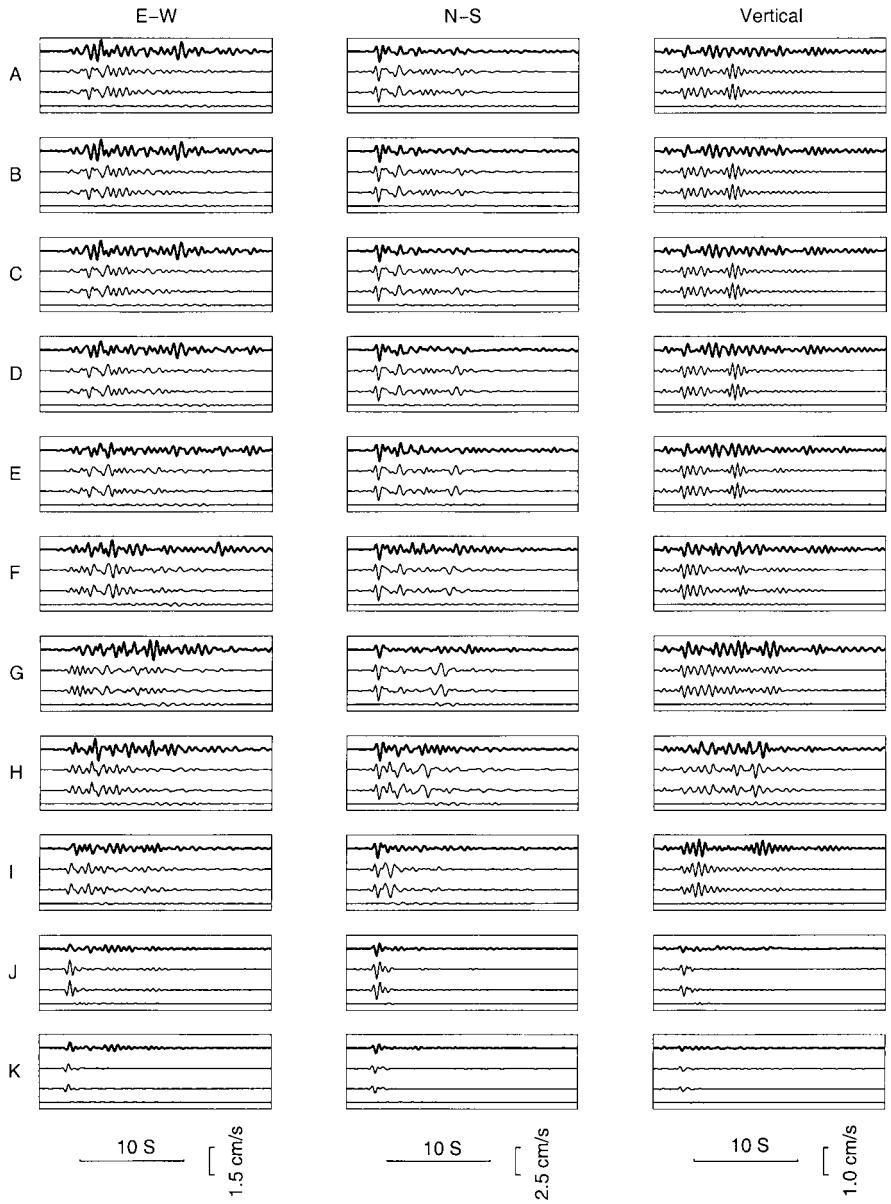

Figure 10. Comparison of simulated velocity seismograms for the **M** 4.9 earthquake to data at 11 surface recording sites (A–K, see Fig. 2a). For each station, the traces from bottom to top show 3D synthetics for the part of the source incident from the North, 3D synthetics for the part of the source incident from below, total 3D synthetics, and data (thick traces).

data at station J for the east–west and vertical components. The peak velocity for data and synthetics are similar at -91 m (in rock), but increases for the synthetics compared to the data toward the surface. The correlation between the strongest (*S*) arrival of the data and synthetics for both surface and borehole records at site J and in particular at the rock site K is very good for the strongest (initial) arrival. However, distinctive phases at about 6–8 sec in the observations are absent in the simulations. The most likely genesis of these phases is the weathered nature of the rock at station K, which was found to be deep (> 30 m) and nonuniform.

Effects of Anelastic Attenuation

We now examine the importance of including anelastic attenuation in the simulations of the **M** 4.9 earthquake. For this purpose, we compute synthetic seismograms in the upper Borrego Valley model with quality factors for both *P* and *S* waves set to 100,000, effectively eliminating the effects of anelastic attenuation. Since the largest amount of energy is incident onto the valley from below, we have omitted the contribution from the waves incident from the North. Figures 15 and 16 compare the simulation to data for the **M** 4.9 earthquake for surface and borehole stations, respec-

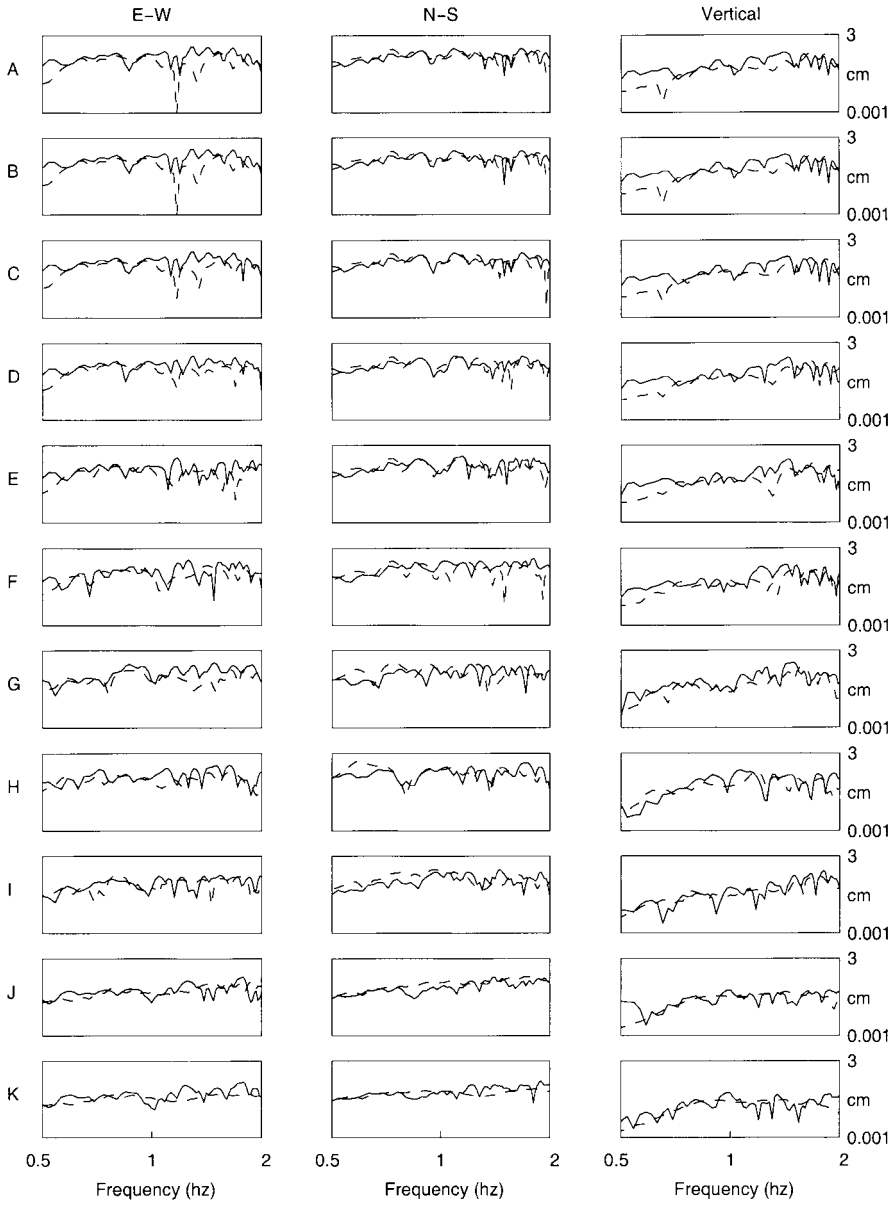

Figure 11. Fourier spectra for the total 3D synthetics (dashed) compared to data (solid) at the surface stations A–K.

tively. While the initial arrivals (3–5 sec) are mostly unaffected by attenuation, the amplitude of the later-arriving waves are grossly overpredicted by the synthetics computed without attenuation. This is in particular the case for the vertical component and for all components at stations located above deeper alluvium (A–H). The effect of attenuation is expectedly much smaller at the rock site (K) and for the stations located above shallow alluvium (I and J).

The anelastic attenuation is clearly most important for the near-surface sediments, in particular for the (unsaturated) alluvium at depths less than about 150 m. Below 150 m at the deep borehole location, the attenuation has a much smaller effect on the ground motion.

2D and 3D Amplification Effects

Due to computer limitations, many seismic hazard studies have been confined to either 1D (e.g. Wong and Silva, 1993; Adan and Rollins, 1993) or 2D modeling (e.g., Vidale and Helmberger, 1988; Hill *et al.,* 1990) and so did not take into account out-of-the-plane propagation and 3D mode conversions. Recent studies that simulate 3D wave propagation suggest significant differences between 1D, 2D and 3D basin model responses (e.g., Horike, 1988; Horike *et al.,* 1990; Frankel, 1993; Olsen and Schuster, 1995). In this section, we examine such differences for the upper Borrego Valley by computing the seismic responses for 1D, 2.5D and 3D models of the valley for the **M** 4.9 event. This comparison

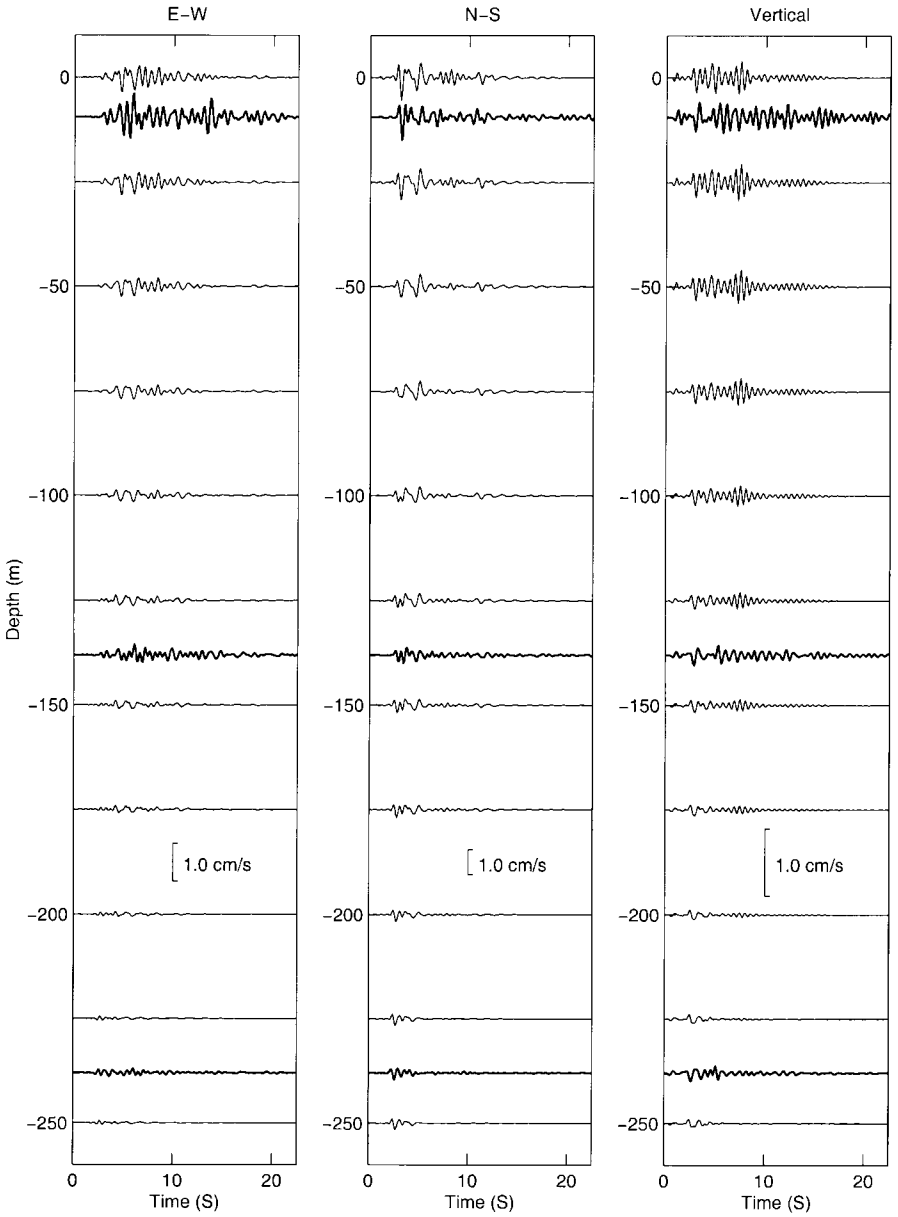

Figure 12. Comparison of simulated seismograms at a depth spacing of 25 m to borehole recordings (thick traces) at 9.4 m, 138 m, and 238 m at the main station for the **M** 4.9 earthquake.

is important, since the outcome of such analyses may show whether the computer extensive 3D modeling is required to accurately estimate ground motion amplification in the upper Borrego Valley, or whether 2D or 1D models suffice.

Figure 17 compares velocity seismograms for 3D, 2.5D and 1D simulations with the **M** 4.9 earthquake for the borehole array at the main station. The model for the 2.5D simulation is a vertical cross section of the 3D upper Borrego Valley model taken along profile A-B shown in Figure 2a. This profile intersects the estimated hypocenter of the earthquake and the main station with the borehole array within 0.5 km. The waves are propagated using the 4th-order 3D finite-difference method, where the 2D cross section was extended in the east-west direction. The 1D model is the layered representation of the 3D upper Borrego Valley model at the main station (see Figure 3). Note the strong similarity between the 1D, 2.5D and 3D responses on the vertical component and the horizontal component with largest amplitude (north–south) for the initial *P* and *S* arrivals. While absent in the 1D synthetics, the 2.5D and 3D simulations reproduce the secondary phase 2–3 seconds after the initial *S* wave on the north–south component, as noticed in the 3D synthetics for the surface array (Fig. 10). However, the 2.5D and in particular the 1D synthetics tend to under-

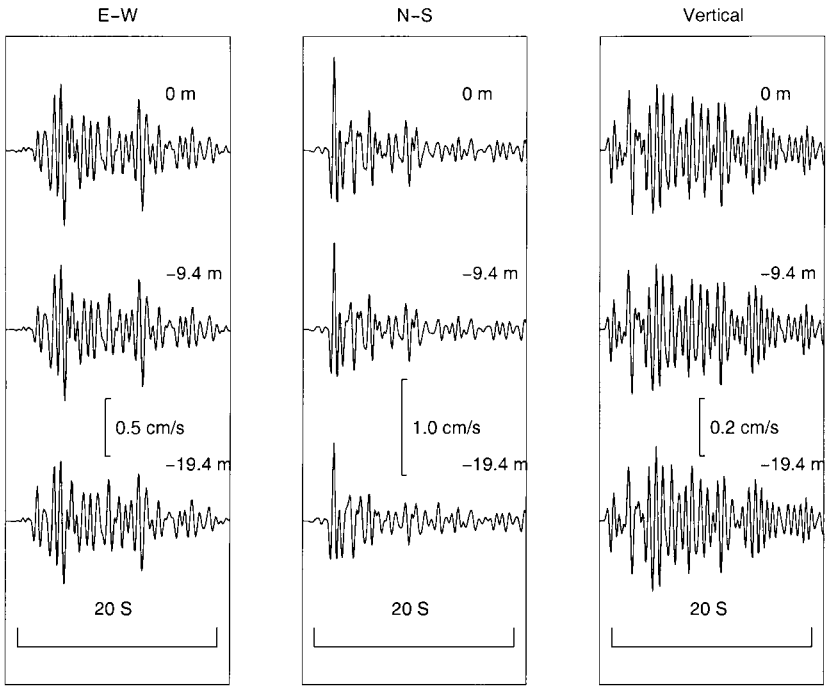

Figure 13. Comparison of borehole recordings of the **M** 4.9 earthquake at depths of 0 m, 9.4 m, and 19.4 m at the main station.

Table 4
Maximum Peak Velocities at Main Station (cm/sec)

Component	Depth (m)	3D	2.5D	1D	Data
East-West	0	0.39	0.11	0.093	0.66
	−19.4	0.35	0.085	0.071	0.55
	−138	0.12	0.049	0.041	0.29
	−238	0.06	0.036	0.029	0.11
North-South	0	0.90	0.89	0.85	0.98
	−19.4	0.71	0.70	0.67	0.81
	−138	0.30	0.29	0.28	0.34
	−238	0.27	0.27	0.27	0.27
Vertical	0	0.24	0.22	0.21	0.23
	−19.4	0.27	0.23	0.22	0.26
	−138	0.11	0.11	0.10	0.15
	−238	0.060	0.058	0.060	0.11

Table 5
Maximum Cumulative Kinetic Energies at Main Station ($J_s \times 10^2$)

Component	Depth (m)	3D	2.5D	1D	Data
East-West	0	1.8	0.09	0.09	3.9
	−19.4	1.4	0.05	0.06	3.7
	−138	1.7	0.02	0.02	0.72
	−238	0.020	0.001	0.000044	0.15
North-South	0	4.5	4.1	2.25	5.0
	−19.4	3.2	3.2	1.58	3.4
	−138	0.74	0.74	0.46	0.97
	−238	0.26	0.29	0.28	0.37
Vertical	0	0.82	0.44	0.20	1.1
	−19.4	0.92	0.42	0.21	1.1
	−138	0.14	0.07	0.05	0.29
	−238	0.03	0.03	0.02	0.13
Total	0	7.1	4.6	2.5	10.0
	−19.4	5.4	3.7	1.9	8.2
	−138	1.1	0.83	0.54	2.0
	−238	0.31	0.32	0.31	0.65

predict the duration on all components, due to insufficient amounts of mode conversion and surface wave generation, and both 1D and 2.5D simulations fail almost completely to generate any of the significant phases on the east-west component. These results are further illustrated in Tables 4 and 5 comparing 1D, 2.5D and 3D peak particle velocities and cumulative kinetic energies, respectively, for the synthetics at the deep borehole array to those for the data.

Conclusions

Our simulation of 2-Hz viscoelastic-wave propagation in a complex 3D model of the upper Borrego Valley reproduces the overall waveforms, peak velocities, cumulative kinetic energies at surface and borehole sites from a nearby **M** 4.9 earthquake within a factor of 2 for most components. The best fit of the synthetics to data is obtained for Q values for P and S waves in the sediments of about 30. Due to the correlation between data and simulation, we are able to identify secondary arrivals in the data as Rayleigh and Love waves generated at the edges and troughs of the basin. The

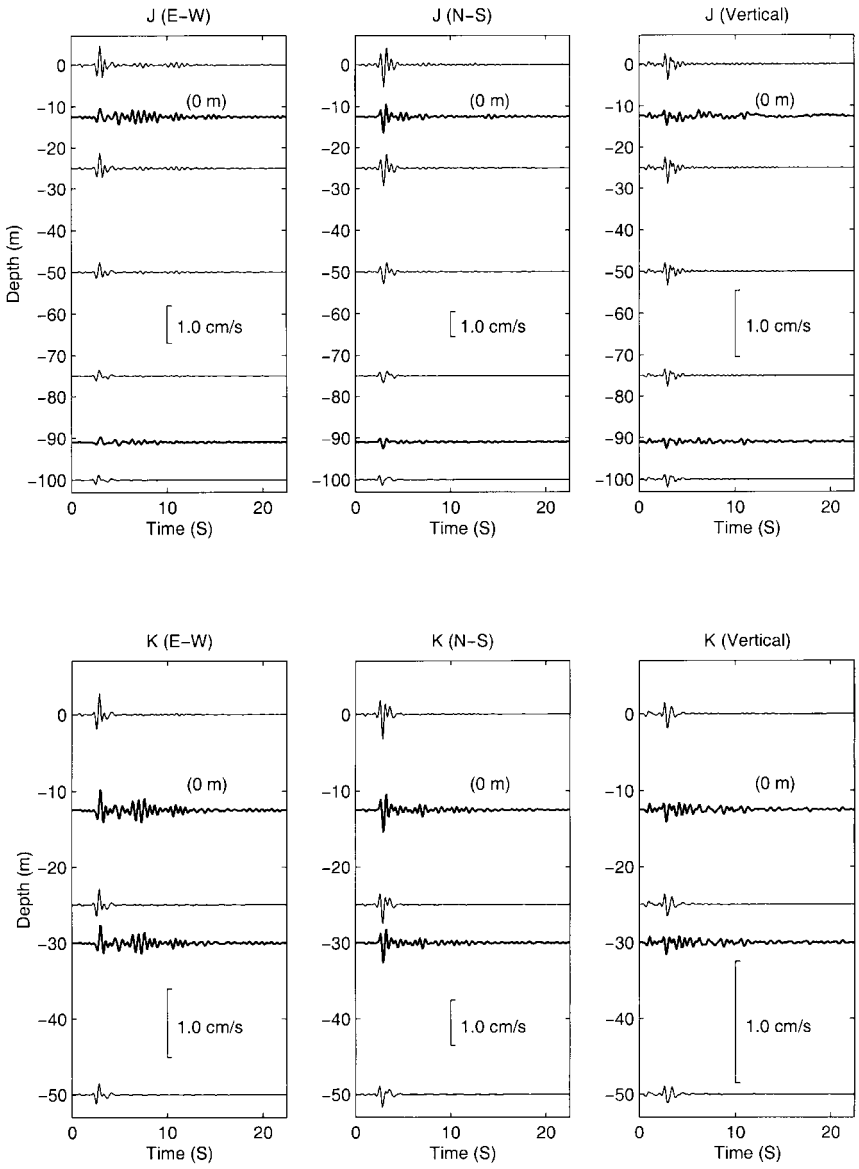

Figure 14. Comparison of simulated velocity seismograms for the **M** 4.9 earthquake at a depth spacing of 25 m to borehole recordings (thick traces) at 0 m and 91 m at station J and at 0 m and 30 m at station K.

largest peak velocities are associated with the north–south component, dominated by the source, along the edges and above some of the deepest parts of the basin, due to focusing and surface-wave generation. The omission of anelastic attenuation in the simulation causes elastic reverberations in the synthetics with amplitudes up to three times larger than those for the viscoelastic model. The peak velocities of the waves incident onto the valley from below are generally more than an order of magnitude larger than those for the waves incident from the North.

We used a profile of the 3D model and the soil parameters at the borehole to examine the ability of 2.5D or 1D model approximations to predict the data. Both 2.5D and 1D model approximations successfully reproduce the peak velocity and cumulative kinetic energy for the total ground motion but underpredict these parameters on some individual components by up to an order of magnitude. Our results suggest that 3D effects from the basin structure, the near-surface low-velocity layer, and attenuation on seismic wave propagation all significantly influence site amplification in the upper Borrego Valley. Future modeling of site amplification in the upper Borrego Valley should include all of these phenomena.

Acknowledgments

This work was supported by Agbabian Associates and by the National Science Foundation under Grant Number EAR-9504866. The Borrego Val-

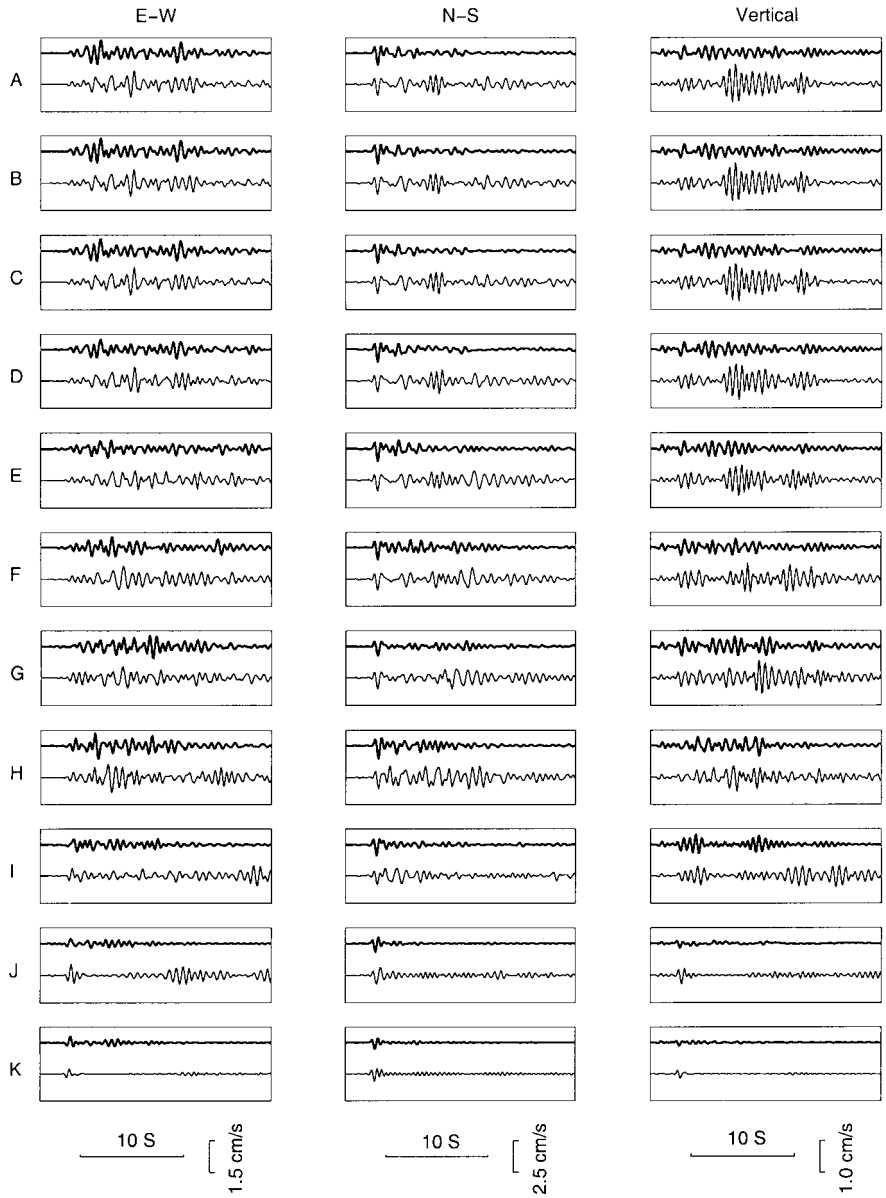

Figure 15. Comparison of simulated (bottom) velocity seismograms for the **M** 4.9 earthquake to data (thick traces) at 11 surface recording sites (A–K, see Figure 2a). The synthetics are computed without anelastic attenuation, and only for the part of the source incident from below.

ley Downhole Array is sponsored by Kajima Corporation and by the Nuclear Power Engineering Corporation of Japan. We thank Harold Magistrale and Tomotaka Iwata for their constructive reviews, which led to an improved manuscript. The computations in this study were carried out on the SGI Origin 2000 at MRL, UCSB (NSF Grant CDA96-01954). This is ICS contribution 0333-86EQ.

References

Adan, S. M., and K. M. Rollins (1993). Damage potential index mapping for Salt Lake Valley, Utah, *Utah Geol. Surv., Misc Pub.* **93–4,** 64 pp.

Agbabian Associates (1996). 3D geophysical studies of the upper Borrego Valley, Report no. 9524-200-004, 20 pp.

Blanch, J. O., J. O. A. Robertsson, and W. W. Symes (1995). Modeling of a constant Q: methodology and algorithm for an efficient and optimally inexpensive viscoelastic technique, *Geophysics* **60,** 176–184.

Cerjan, C., D. Kosloff, R. Kosloff, and M. Reshef (1985). A nonreflecting boundary condition for discrete acoustic and elastic wave equations, *Geophysics* **50,** 705–708.

Clayton, R., and B. Engquist (1977). Absorbing boundary conditions for acoustic and elastic wave equations, *Bull. Seism. Soc. Am.* **71,** 1529–1540.

Frankel, A., and J. Vidale (1992). A three-dimensional simulation of seismic waves in the Santa Clara Valley, California, from a Loma Prieta aftershock, *Bull. Seism. Soc. Am.* **82,** 2045–2074.

Frankel, A. (1993). Three-dimensional simulations of ground motions in the San Bernardino Valley, California, for hypothetical earthquakes on the San Andreas Fault, *Bull. Seism. Soc. Am.* **83,** 1020–1041.

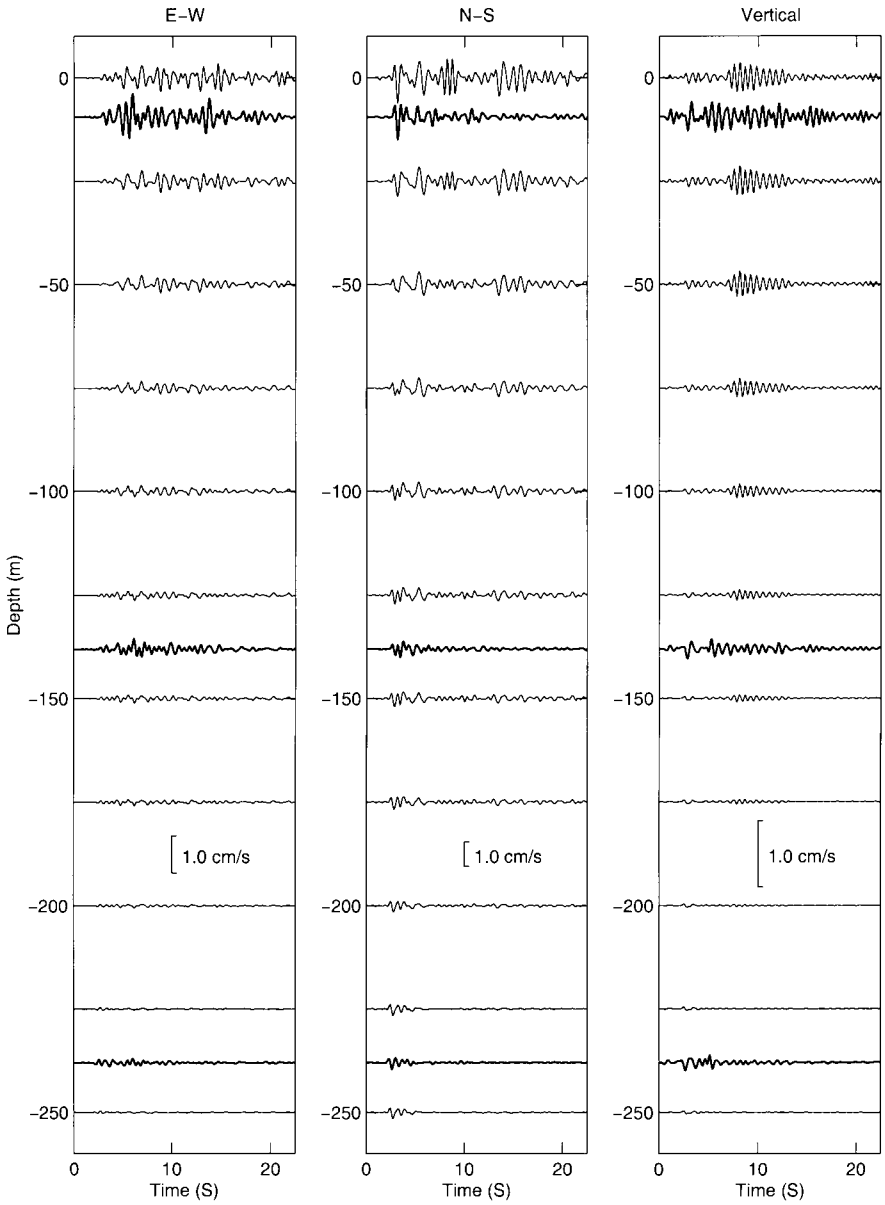

Figure 16. Same as Figure 11, but for 3D synthetics computed without anelastic attenuation.

Graves, R. W. (1996). Simulating seismic wave propagation in 3D elastic media using staggered-grid finite differences, *Bull. Seism. Soc. Am.* **86,** 921–924.

Hadley, D., and H. Kanamori (1977). Seismic structure of the Transverse Ranges, California, *Geol. Soc. Am. Bull.* **88,** 1469–1478.

Hill, J., H. Benz, M. Murphy, and G. T. Schuster, (1990). Propagation and resonance of SH waves in the Salt Lake Valley, Utah, *Bull. Seism. Soc. Am.* **80,** 23–42.

Horike, M. (1988). Analysis and simulation of seismic ground motions observed by an array in a sedimentary basin, *J. Phys. Earth* **36,** 135–154.

Horike, M., H. Uebayashi, and Y. Takeuchi (1990). Seismic response in three-dimensional sedimentary basin due to plane S wave incidence, *J. Phys. Earth* **38,** 261–284.

Levander, A. R. (1988). Fourth-order finite-difference P-SV seismograms, *Geophysics* **53,** 1425–1436.

Olsen, K. B. (1994). Simulation of three-dimensional wave propagation in the Salt Lake Basin, Ph.D. Thesis, University of Utah.

Olsen, K. B. (1999). Site amplification in the Los Angeles basin from 3D modeling of ground motion, *Bull. Seism. Soc. Am.* (submitted).

Olsen, K. B. and R. J. Archuleta (1996). Three-dimensional simulation of earthquakes on the Los Angeles fault system, *Bull. Seism. Soc. Am.* **86,** 575–596.

Olsen, K. B., and G. T. Schuster (1994). Three-dimensional modeling of site amplification in east Great Salt Lake basin, *USGS Technical Report 1434-93-G-2345.*

Olsen, K. B., and G. T. Schuster (1995). Causes of low-frequency ground motion amplification in the Salt Lake Basin: the case of the vertically-incident *P* wave, *Geophys. J. Int.* **122,** 1045–1061.

Olsen, K. B., J. C. Pechmann, and G. T. Schuster (1995a). Simulation of 3D elastic wave propagation in the Salt Lake Basin, *Bull. Seism. Soc. Am.* **85,** 1688–1710.

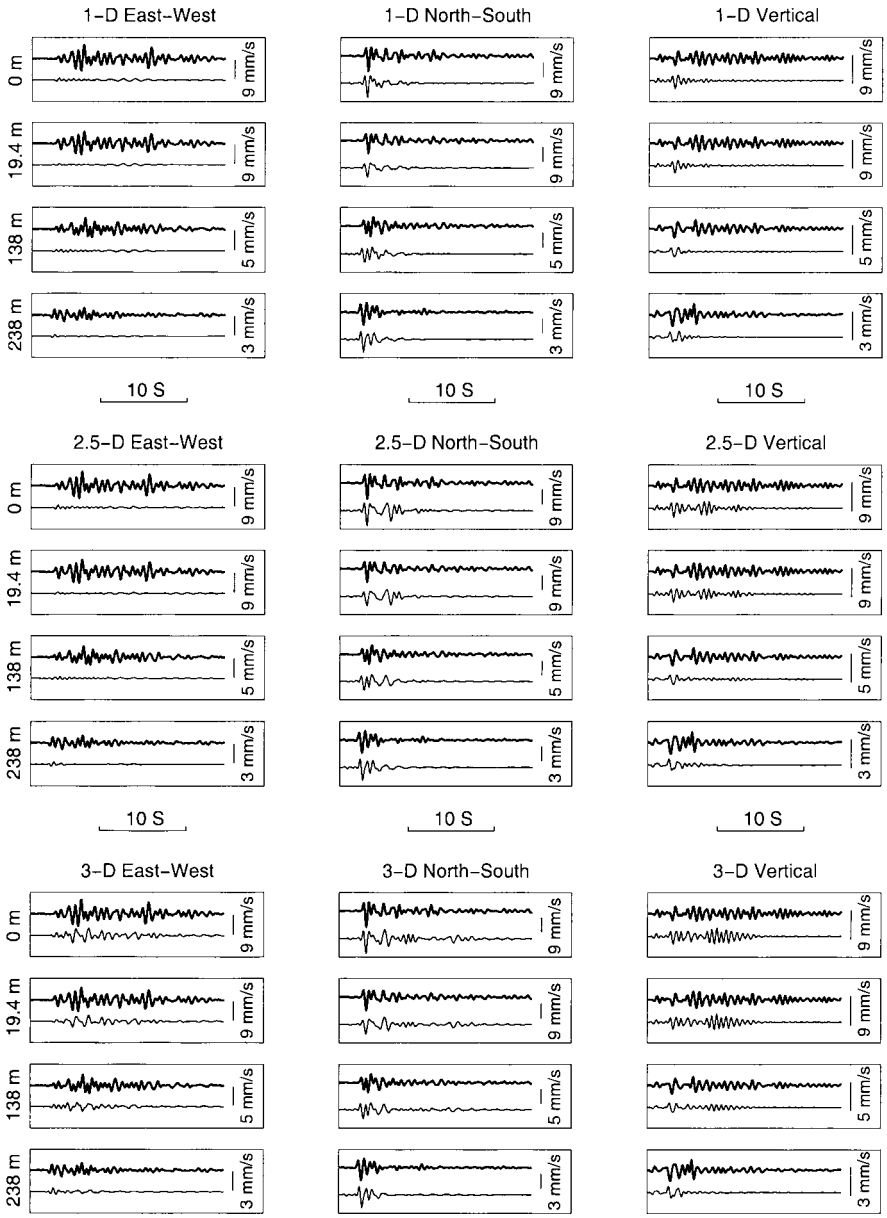

Figure 17. Comparison of 3D, 2.5D, and 1D synthetics with data (thick traces) at the deep borehole array.

Olsen, K. B., R. J. Archuleta, and J. R. Matarese (1995b). Three-dimensional simulation of a magnitude 7.75 earthquake on the San Andreas fault, *Science* **270,** 1628–1632.

Olsen, K. B., J. C. Pechmann, and G. T. Schuster (1996). An analysis of simulated and observed blast records in the Salt Lake Basin, *Bull. Seism. Soc. Am.* **86,** 1061–1076.

Robertsson, J. O. A., J. O. Blanch, and W. W. Symes (1994). Viscoelastic finite-difference modeling, *Geophysics* **59,** 1444–1456.

Steidl, J., A. Tumarkin, and R. J. Archuleta (1996). What is a reference site? *Bull. Seism. Soc. Am.* **86,** 1733–1748.

Vidale, J. E., and D. V. Helmberger (1988). Elastic finite-difference modeling of the 1971 San Fernando, California earthquake, *Bull. Seism. Soc. Am.* **78,** 122–141.

Wald, D. J., and R. W. Graves (1998). The seismic response of the Los Angeles Basin, California, *Bull. Seism. Soc. Am.* **88,** 337–356.

Wong, I. G., and W. J. Silva (1993). Site-specific strong ground motion estimates for the Salt Lake Valley, Utah, *Utah Geol. Surv., Misc. Pub.* **93–9,** 34 pp.

Yomogida, K., and J. T. Etgen (1993). 3D wave propagation in the Los Angeles Basin for the Whittier-Narrows Earthquake, *Bull. Seism. Soc. Am.* **83,** 1325–1344.

Institute for Crustal Studies
UC Santa Barbara, Santa Barbara, CA 93106-1100
(K.B.O.)

Dept. of Civil Engineering
USC, Los Angeles, CA 90089-2531
(R.N.)

Kajima Corporation, 6-5-30, Akasaka, Minato-ku,
Tokyo 107, Japan
(T.K.)

Manuscript received 15 April 1999.